
FOUNDATION MODELS FOR SEISMIC DATA PROCESSING: AN EXTENSIVE REVIEW

A PREPRINT

✉ Fabian Fuchs^{*1,2}, ✉ Mario Ruben Fernandez¹, Norman Ettrich¹, and ✉ Janis Keuper^{2,3}

¹Fraunhofer-Institut für Techno- und Wirtschaftsmathematik

²DWS, University of Mannheim

³IMLA, Offenburg University

April 1, 2025

ABSTRACT

Seismic processing plays a crucial role in transforming raw data into high-quality subsurface images, pivotal for various geoscience applications. Despite its importance, traditional seismic processing techniques face challenges such as noisy and damaged data and the reliance on manual, time-consuming workflows. The emergence of deep learning approaches has introduced effective and user-friendly alternatives, yet many of these deep learning approaches rely on synthetic datasets and specialized neural networks. Recently, foundation models have gained traction in the seismic domain, due to their success in natural imaging. This paper investigates the application of foundation models in seismic processing on the tasks: demultiple, interpolation, and denoising. It evaluates the impact of different model characteristics, such as pre-training technique and neural network architecture, on performance and efficiency. Rather than proposing a single seismic foundation model, this paper critically examines various natural image foundation models and suggest some promising candidates for future exploration.

1 Introduction

Seismic processing is essential for converting raw data into high-quality subsurface images. Precise subsurface imaging is vital for various geoscience applications, such as sedimentary and tectonic interpretation, hydrocarbon exploration, reservoir analysis, and geothermal characterization [Yilmaz and Doherty, 2001]. The challenges associated with this process include environmental noise, damaged geophones, and weak low-frequency signals, which degrade data accuracy. Therefore, this transformation involves complex processing steps to enhance the quality of the data. While these techniques improve the quality and accuracy of seismic images, they often rely on time-consuming workflows that approximate the physics behind wave propagation. Additionally, these techniques frequently require manual processes like picking velocities and mute functions, as well as parameter tuning, generally involving iterative trial-and-error adjustments based on the dataset, such as discriminating multiples and primaries in the Radon domain [Trad et al., 2003]. Therefore, seismic processing requires significant human expertise to extract geological and physical information while mitigating undesired artifacts inherent in the data or introduced by the processing.

In recent years, motivated by the success of deep learning (DL) approaches in computer vision (CV), DL based approaches have emerged as effective, parameter-free, and user-friendly alternatives to traditional seismic processing techniques [Mousavi and Beroza, 2022]. Recent studies have successfully applied DL based approaches to seismic data interpolation, denoising, deblending, ground-roll

*fabian.fuchs@itwm.fraunhofer.de

attenuation, velocity picking, and dispersion curve estimation (Chai et al. [2020], Fernandez et al. [2022a], Fernandez et al. [2022b], Mandelli et al. [2019], Birnie et al. [2021], Qiu et al. [2022], Zhang et al. [2019], Wang et al. [2021a], Guo et al. [2020], Kaur et al. [2020], Wang et al. [2021b], Chamorro et al. [2024]). However, the majority of these DL based solutions are specialized neural networks trained for a single specific task.

In contrast, foundation models (FMs) are large neural networks that have been pre-trained on vast amounts of data in order to be used in a wide range of downstream tasks. This approach has recently led to numerous breakthroughs across diverse domains, including: ChatGPT [Brown et al., 2020] in the natural language processing domain, SAM [Kirillov et al., 2023] in image segmentation, Stable Diffusion [Rombach et al., 2022] in image generation, SORA [Liu et al., 2024] in video generation and more relevantly for seismic processing, image encoders, such as Vision Transformer (ViT) [Dosovitskiy et al., 2020], ConvNeXt [Liu et al., 2022a] and Swin Transformer (Swin) [Liu et al., 2021] in CV.

The success of DL based approaches in seismic and the achievements of FMs in CV have prompted a surge of research interest in seismic foundation models (SFMs). Currently, most DL approaches for seismic applications rely on synthetic data, due to the difficulties in labeling field seismic data. This presents a challenge, as synthetic datasets often fail to capture the true diversity and characteristics of field seismic data. A key benefit of SFMs is their ability to be pre-trained on and learn from seismic field data before being fine-tuned on synthetic data for the specific downstream tasks, as shown in Figure 1. The ability to learn directly from seismic field data, in combination with larger neural networks inherent to FM, promises improved performance and even more importantly better generalization.

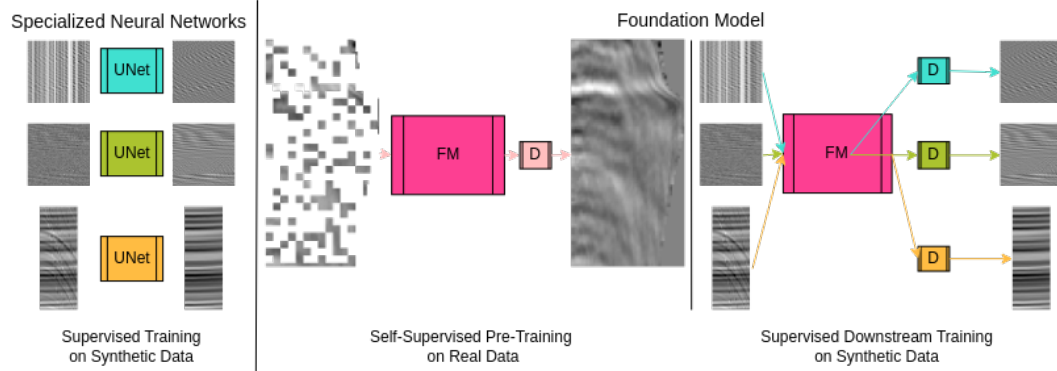


Figure 1: Comparison between specialized neural networks and FMs. Specialized neural networks, like UNets, are trained end to end for each downstream task. In comparison, an FM is pre-trained once and then fine-tuned for each downstream task. The pre-training is done through self-supervised learning on real field data and the fine-tuning through supervised learning on synthetic data. The parts of the model denoted as D are task dependent decoders.

1.1 FMs in geophysics

Although the term FM is not explicitly used, StorSeismic from Harsuko and Alkhalifah [2022] is one of the first reported SFM. StorSeismic utilizes a Bidirectional Encoder Representations from Transformers (BERT) model, as outlined in Devlin et al. [2019]. It is first pre-trained on a mixture of real and synthetic data seismic data and subsequently fine-tuned for different downstream tasks.

In the field of seismic processing, StorSeismic employs a distinctive approach by treating each trace as a word, and a gather as a sentence. This strategy is supported by BERT, a model specifically engineered for natural language processing. In contrast, a more prevalent strategy within the seismic processing domain involves treating the gather as an image and leveraging models from the natural image domain. This approach is used by Sheng et al. [2024], Pham et al. [2025] and Sansal et al. [2025], who all utilize a ViT [Dosovitskiy et al., 2020] as an image encoder. All three adopt the masked autoencoders (MAE) framework [He et al., 2021], which trains an encoder-decoder model

via self-supervision. This process entails masking part of the input gather and training the model to recreate the whole gather. Following this pre-training phase, the encoder component of the model is employed as a feature extractor for a range of downstream tasks. A notable distinction between the approach presented by Sansal et al. [2025] and the other two image-based approaches is, that the former uses three-dimensional seismic data, which is a more complex problem.

Another image-based approach is the generative seismic foundation model (GSFM) [Cheng et al., 2025], which utilizes a diffusion model. In contrast, to the SFMs previously mentioned, which pre-train a feature extractor and then train specific decoders for different downstream tasks, their GSFM is pre-trained and fine-tuned for all their downstream tasks simultaneously. This enables them to share the whole network, not just the image encoder, between downstream tasks.

1.2 Motivation

The majority of the image-based approaches previously referenced, except Cheng et al. [2025], use a ViT as their image encoder. While ViTs have been extensively utilized in the domain of natural images, there is a need to assess their suitability for the domain of seismic processing. This is particularly salient in light of recent studies by Goldblum et al. [2023], which empirically demonstrate that ViTs may not be the optimal architecture even for all natural image applications. Therefore, there is a need for comparing and benchmarking other FMs for seismic processing.

In this paper, we conduct a comprehensive investigation into various FMs and develop a framework for further testing. We assess the performance of the different FMs on three seismic processing tasks: demultiple, interpolation, and denoising. For the latter two tasks, we utilize an open-source dataset, which, when combined with the source code that will be made available, allows for the reproduction of our results and serves as a foundation for further research. We quantitatively evaluate a diverse range of FMs using synthetic data, aiming to clarify how various model characteristics, such as pre-training techniques and architectural design choices, impact their performance. Additionally, we select a subset of models for qualitative assessment, where we present demultiple results of real field data. Finally, we aim to investigate the impact of natural image pre-training, because unlike curated seismic data sets, extensive natural image datasets are widely available.

2 Methodology

The encoder-decoder architecture, illustrated in Figure 2, serves as the foundation of our framework developed to benchmark a broad variety of FMs.

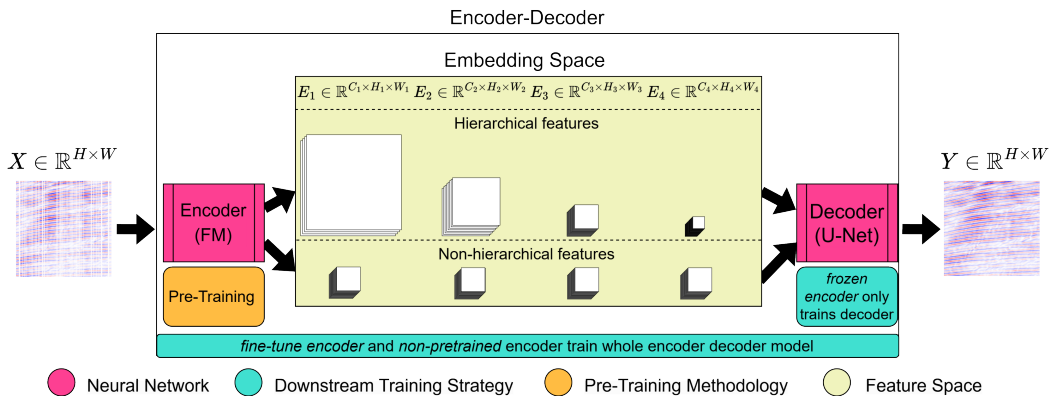


Figure 2: Depiction of the architecture of the encoder-decoder model with an arbitrary FM, that produces a four-stage feature map, as the image encoder and a UNet-style decoder. Also represented are both hierarchical and non-hierarchical features. Additionally, the components of the encoder-decoder network that are affected by pre-training and the components that are affected by the different downstream training strategies are labeled.

We define an encoder-decoder model as the composition $\mathcal{D}_{\theta_D} \circ \mathcal{E}_{\theta_E}$ of an encoder (2) and a decoder (3). Each of them is parametrized by some parameters θ and together this composition approximates a real underlying function f (1). This function maps from a two-dimensional space X of height H and width W into another two-dimensional space Y of the same height and width. While we assume two-dimensional input and output spaces of the same size, neither changing the sizes nor adding dimensions fundamentally alters the problem.

$$f : X \in \mathbb{R}^{H \times W} \mapsto Y \in \mathbb{R}^{H \times W} \quad (1)$$

$$\mathcal{E}_{\theta_E} : X \in \mathbb{R}^{H \times W} \mapsto \{E_s : E_s \in \mathbb{R}^{C_s \times H_s \times W_s} \quad \forall \quad 1 \leq s \leq S\} \quad (2)$$

$$\mathcal{D}_{\theta_D} : \{E_s : E_s \in \mathbb{R}^{C_s \times H_s \times W_s} \quad \forall \quad 1 \leq s \leq S\} \mapsto Y^* \in \mathbb{R}^{H \times W}, Y^* \approx Y \in \mathbb{R}^{H \times W} \quad (3)$$

As defined in Equation (2), the encoder outputs a set of embeddings. Each embedding E_s is an element of a three-dimensional space, with C_s channels, a height of H_s and a width of W_s . The total number of embeddings S depends on the architecture and number of skip-connections. A neural network without skip-connections only uses one embedding as embedding space and a neural network with skip-connections, such as a UNet, uses multiple embeddings. We define an encoder as non-hierarchical, if all embeddings have the same spatial dimensions, as defined in Equation (4). In contrast, a hierarchical model has embeddings at varying resolutions.

$$\mathcal{E}_{\theta_E} := \begin{cases} \text{non-hierarchical,} & \text{if } H_i = H_j \quad \forall \quad 1 \leq i < j \leq S \\ & \wedge W_i = W_j \quad \forall \quad 1 \leq i < j \leq S \\ \text{hierarchical,} & \text{otherwise} \end{cases} \quad (4)$$

As illustrated in Figure 2, our encoder-decoder architecture uses four embeddings. The choice of four stages is motivated by the fact that most hierarchical models, that we compared in this study, have four distinct stages.

An FM is a model that has been pre-trained on a vast dataset and is then used for several distinct downstream tasks. One possible pre-training method is self-supervised learning as outlined in Equation (5). We chose self-supervised learning as the example, because is the most probable pre-training method for an SFM and was already used by Sheng et al. [2024], Pham et al. [2025] and Sansal et al. [2025]. It should be noted though, that other pre-training methods exist. We will discuss some of them later in Section 2.1.1.

$$\begin{aligned} \text{self-supervised pre-training} &:= \min_{\theta_E^{PT}, \theta_D^{PT}} \sum_{i=0}^N L(X_i^*, X_i) \\ &:= \min_{\theta_{EPT}, \theta_{DPT}} L_{ss}(\mathcal{D}_{\theta_D^{PT}}(\mathcal{E}_{\theta_E^{PT}}(X_i^M)), X_i) \end{aligned} \quad (5)$$

For self-supervised learning, as outlined in Equation (5) the mapping changes from $X \mapsto Y$ to $X^M \mapsto X$, with X being our data, such as natural images or seismic field data and X^M being a randomly masked version of X . Consequently, X^* is the prediction of the encoder-decoder network ($X^* := \mathcal{D}_{\theta_D^{PT}}(\mathcal{E}_{\theta_E^{PT}}(X^M))$). Additionally, L_{ss} is a pixel based loss, such as ℓ_1 or ℓ_2 , with the specific loss depending on the implementation. It is important to note, that while an encoder-decoder network is used during pre-training only the encoder is the FM, as defined in Equation (6). Therefore, the decoder is kept as small as possible ($|\theta_D^{PT}| \ll |\theta_E^{PT}|$) shifting more responsibility to the encoder to create more meaningful features.

$$FM_{\theta_E^{PT}} := \text{Encoder}_{\theta_E^{PT}} \quad (6)$$

Pre-training with self-supervision can be done on real data. However, downstream training, as outlined in Equation (7), often relies on supervised learning, which, in seismic processing, involves the use of synthetic data, with X representing the input, Y the label, and Y^* the prediction of the model ($Y^* := \mathcal{D}_{\theta_D}(FM_{\theta_E| \theta_E^{PT}}(X))$). Similar to self-supervised learning, during supervised learning

any pixel based loss can be used for L_s . However, based on some initial experiments and the findings by Zhao et al. [2017] we decided on the ℓ_1 for our downstream training.

$$\begin{aligned} \text{supervised downstream training} &:= \min_{\theta_E|\theta_E^{PT},\theta_D} \sum_{i=0}^N L_s(Y_i^*, Y_i) \\ &:= \min_{\theta_E|\theta_E^{PT},\theta_D} \sum_{i=0}^N L_s(\mathcal{D}_{\theta_D}(FM_{\theta_E|\theta_E^{PT}}(X_i)), Y_i) \end{aligned} \quad (7)$$

Importantly, the downstream training is performed separately for each distinct task. For our downstream training, we use a decoder inspired by the right side of a UNet [Ronneberger et al., 2015]. The UNet is a convolutional neural network (CNN) originally designed for biomedical image segmentation. It consists of an encoder-decoder structure with skip-connections. The encoder progressively reduces the spatial dimensions while increasing the feature depth, capturing context. The decoder then upsamples the feature maps to reconstruct the original image size, using skip connections from the encoder to retain high-resolution details. In our context, the encoder is replaced by an FM and only the decoder part is kept, as illustrated in Figure 2 and defined in Equation (7). The four stage feature maps produced by the FM are used as intermediate representations and then fed to the decoder. Therefore, the decoder has to adapt its channel size and upsampling factor to these feature maps.

The reason for choosing a UNet structure is its effectiveness in pixel-level regression tasks, such as the seismic processing tasks we consider. This robustness was demonstrated multiple times, for example by Fernandez et al. [2025] for demultiple, by Fernandez et al. [2022b] and Chai et al. [2020] for interpolation, by Zhang et al. [2019] for denoising and by Cheng et al. [2025] who used a UNet as basis for their GSFM. While the focus of this study are FMs and therefore the encoder, some additional details and investigations about the decoder and its design can be found in Appendix A.2.

2.1 Models

In order to select an architecture that is optimal for seismic processing tasks, a broad variety of FMs were compared. These FMs can be categorized into two groups: hierarchical and non-hierarchical models, as defined in Equation (4). In addition, we compared their architecture and their pre-training method. The architecture can either be convolutional-, transformer- or hybrid based and the different pre-training methods are explained in the next section. All the models, compared in this study, as well as their characteristics are summarized in Table 1. The selection of models was chosen to cover a broad range of distinct models with minimal overlap in their characteristics.

2.1.1 Pre-Training Methods

The investigated models vary not only in their architecture but also in their pre-training method. Observed methods include supervised, self-supervised, self-supervised with distillation, semi-supervised, multitask and contrastive learning. Short introductions to each method are provided below, with further details available in their references.

Supervised learning is the most common training method and involves the use of labeled datasets and the prediction of these labels. In this context, this entails the utilization of a version of ImageNet [Russakovsky et al., 2015] and the prediction of the class of each image.

Self-supervised learning, in contrast to supervised-learning, utilizes unlabeled image datasets. In this context, a concrete form of self-supervised learning called Masked Image Modeling (MIM) [Bao et al., 2022] is used. During training part of the image is masked, and the network has to recreate the image or predict the missing patches. The advantage is that unlabeled image datasets can be used. Furthermore, recreating the image is a more involved task than classification, which leads to more generalizable features.

Self-supervised learning with distillation, as used by Oquab et al. [2024] uses a teacher network, typically significantly larger than the student network, to teach the student to predict the outputs from the teacher. These outputs are a probability distribution over the target classes. By learning to predict the complete probability distribution of the teacher instead of just the correct label, the knowledge representation of the teacher model is distilled into the student model [Hinton et al., 2015]. This is

Model	Hierarchical	Architecture	Pre-Training	Citation
CAFormer 	yes	Hybrid	SL 	Yu et al. [2024]
ConvNeXt 	yes	Convolutional	SL 	Liu et al. [2022a]
ConvNeXt 	yes	Convolutional	CL 	Liu et al. [2022a]
ConvNeXt(V2) 	yes	Convolutional	SSL 	Woo et al. [2023]
DaViT 	yes	Transformer	MTL 	Ding et al. [2022]
DeiT III 	no	Transformer	SL 	Touvron et al. [2022]
Dino 	no	Transformer	SSLD 	Oquab et al. [2024]
EfficientNet 	yes	Convolutional	Semi-S 	Tan and Le [2020]
EVA02 	no	Transformer	SSL 	Fang et al. [2024]
EVA02 	no	Transformer	CL 	Fang et al. [2024]
Hiera 	yes	Transformer	SSL 	Ryali et al. [2023]
MambaOut 	yes	Convolutional	SSL 	Yu and Wang [2024]
Swin 	yes	Transformer	SL 	Liu et al. [2021]
Swin (V2) 	yes	Transformer	SSL 	Liu et al. [2022b]
ViTamin 	yes	Hybrid	CL 	Chen et al. [2024]

Table 1: Overview and categorization of the investigated models. For the pre-training strategy SL stands for supervised learning, SSL for self-supervised learning, SSLD for self-supervised learning with distillation, Semi-S for semi-supervised learning, MTL for multitask learning and CL for contrastive learning. The color next to the model denotes the model archetype, and in conjunction with the shape next to the pre-training strategy, this combination constitutes the legend for the majority of the figures in Section 3.

important because the smaller model may have insufficient capacity to learn this representation on their own.

Semi-supervised training refers to the Noisy Student Training introduced in Xie et al. [2020]. It has three main steps: training a teacher on labeled images, using the teacher to generate pseudo labels on unlabeled data, training a student on a combination of labeled and unlabeled data. This process is iterated by switching the student to the teacher and training a new student. This approach not only delivers better accuracy but also better generalization than supervised training. Additionally, similar to self-supervised training this method can benefit from vast unlabeled datasets. In contrast to self-supervised learning with distillation, only the pseudo labels are predicted and not the whole probability distribution of the teacher. A similar iterative approach, but without training multiple networks, was used by Cheng et al. [2025] to shift their network from synthetic data to real data.

Multitask learning references the training employed in Xiao et al. [2024] and combines image-level, pixel-level and semantic tasks. Image-level tasks involve comprehending the overall context of an image and the semantic relationships, with tasks like image classification, captioning, and visual question answering. Pixel level tasks focus on object and entity localization within images and understanding their relationships and spatial context, including object detection and segmentation. Semantic tasks require a detailed understanding of both text and image to align image regions with corresponding text phrases, challenging the model to grasp local details and semantic contexts. In contrast, to the pre-training methods mentioned before, multitask learning is not image to image based, but requires a combination of image and text prompt as input and delivers a text prompt as output. One disadvantage of this approach is that it requires an annotated dataset.

Finally, contrastive learning [Radford et al., 2021] aims to learn a shared feature space for images and text. To achieve this a text encoder and image encoder are trained together to minimize the cosine similarity between correct (text, image) pairings and maximize the distance between incorrect pairings. One disadvantage of this approach, similar to multitask learning, is that it requires an annotated dataset. On the other hand this approach enables zero- and few-shot classification, not limited by the number of classes used during training. Furthermore, models pre-trained with contrastive learning enabled breakthroughs in image retrieval and search. Not only is it possible to search images based on text, but also text based on images.

The majority of the models examined in this study have a corresponding pre-training method, with exceptions being ConvNeXt and Swin. Both are available pre-trained with supervision and self-supervision (both models have a V2 version of the model for self-supervision with only minimal architectural changes). Additionally, ConvNeXt (in its V1 variant) is available with contrastive learning as pre-training strategy. Furthermore while DEiT3, DINO and EVA02 are distinct models, fundamentally they are all a ViT with their biggest difference being their pre-training method. The corresponding pre-training method for each tested model is declared in Table 1.

2.2 Downstream Training Strategies

In addition to the aforementioned models, this study compares three distinct downstream training strategies, as outlined in Figure 3. These training strategies differ from the pre-training methods mentioned above. While the pre-training method defines how the FMs, which are used as image encoders, were pre-trained, the subsequent training strategies describe how the entire encoder-decoder model is trained for down-stream seismic applications.

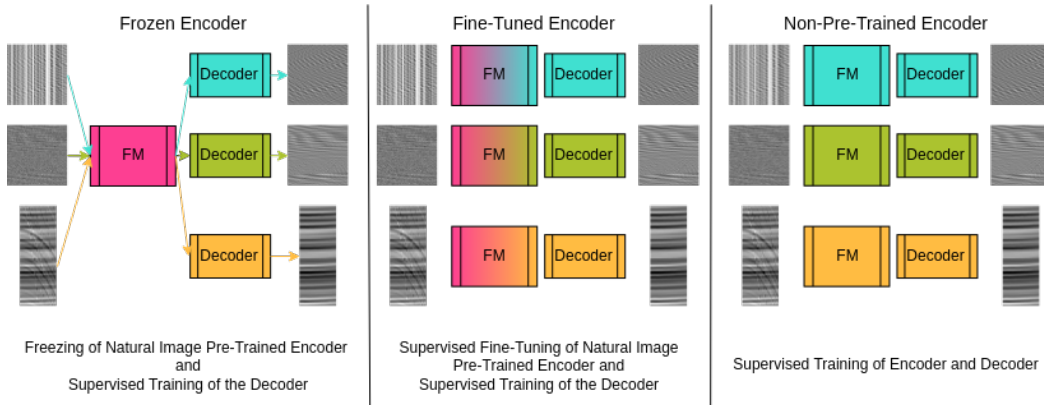


Figure 3: Comparison of the different downstream training strategies. *Frozen encoder* freezes a natural image pre-trained FM and only trains the decoder. *Fine-tuned encoder* fine-tunes a natural image pre-trained FM and trains the decoder. *Non-pre-trained encoder* trains the whole encoder-decoder model from scratch. While all three downstream training strategies use supervised training, the pre-training method differs. Which specific pre-training method is used, is noted in Table 1. Additionally, a short introduction about each observed pre-training method can be found in Section 2.2.

The first strategy, dubbed *frozen encoder* employs FMs pre-trained on natural images directly (freezes the encoder) and only trains the decoder to adapt the output features of the FM for seismic processing tasks, as defined in Equation (8). As described in the equation, freezing the encoder means that the parameters of the encoder stay untouched and are not further optimized. Analogue to Equation (7), X is our input, Y are our labels, Y^* are the predictions of the encoder-decoder network and L_s is the ℓ_1 loss.

$$\begin{aligned} \text{frozen encoder} &:= \min_{\theta_D} \sum_{i=0}^N L_s(Y_i^*, Y_i) \\ &:= \min_{\theta_D} \sum_{i=0}^N L_s(\mathcal{D}_{\theta_D}(FM_{\theta_{E^{PT}}}(X_i)), Y_i) \end{aligned} \quad (8)$$

The second strategy, designated *fine-tuned encoder*, uses the same FMs pre-trained on natural images. However, rather than freezing the pre-trained weights, it fine-tunes them, as well as training the decoder, as demonstrated in Equation (9).

$$\begin{aligned}
 \text{pre-trained encoder} &:= \min_{\theta_E | \theta_E^{PT}, \theta_D} \sum_{i=0}^N L_s(Y_i^*, Y_i) \\
 &:= \min_{\theta_E | \theta_E^{PT}, \theta_D} \sum_{i=0}^N L_s(\mathcal{D}_{\theta_D}(FM_{\theta_E | \theta_E^{PT}}(X_i)), Y_i)
 \end{aligned} \tag{9}$$

The third strategy *non-pre-trained encoder* also employs the same neural networks but without their pre-trained weights. Instead, the whole encoder-decoder is randomly initialized and then trained from scratch for each specific downstream task, as demonstrated in Equation (10).

$$\begin{aligned}
 \text{non-pre-trained encoder} &:= \min_{\theta_E, \theta_D} \sum_{i=0}^N L_s(Y_i^*, Y_i) \\
 &:= \min_{\theta_E, \theta_D} \sum_{i=0}^N L_s(\mathcal{D}_{\theta_D}(\mathcal{E}_{\theta_E}(X_i)), Y_i)
 \end{aligned} \tag{10}$$

In most of the experiments, the strategy *frozen encoder* was employed because it is significantly cheaper to compute. This is because the encoder, which corresponds to upwards of 80% of the whole encoder-decoder model, is frozen and not trained. Our hypothesis is that the transfer learning capability of the network is indicative of the performance of the network for seismic pre-training. Furthermore, we aim to investigate the impact of natural image pre-training. Natural image datasets, unlike curated seismic data sets, are extensive. Furthermore, due to solely training the decoder the training takes hours instead of days, thereby enabling the assessment of a greater number of FMs.

Given the substantial number of potential combinations of FMs and downstream tasks, it was not feasible to conduct individual hyperparameter optimizations for each combination. Instead, the experiments utilized a set of fixed hyperparameters, which included AdamW as the optimizer, a learning rate of 0.001, a constant learning rate scheduler, and a weight decay of 0.01. The only difference of the hyperparameters between the downstream tasks was the number of epochs, with 50 epochs selected for the demultiple task and 100 epochs for the other two downstream tasks. This is due to latter two using a random cut augmentation and therefore diversifying the data more between epochs. Further details can be found in the source code.

3 Results

In order to draw comparisons between the various FMs, it is necessary to consider a number of different dimensions. The primary and most significant of these is the architecture, which can be roughly divided into hierarchical and non-hierarchical models, as well as transformer-, convolution- and hybrid-based approaches. The categorization of the models was discussed in Section 2.1. Another differentiating factor is the pre-training strategy, which is predominantly interesting from a transfer learning perspective and to a lesser extent to the training of a seismic processing FM. This is due to the fact that the majority of pre-training strategies are not applicable to the seismic processing domain. A more relevant aspect, is the pre-training dataset size used, as this provides insight into the amount of data required to train an FM for seismic processing. The final dimensions that will be examined in this study are model size and inference time, as well as the size of the embedding space. These are crucial because an SFM must be efficient enough to handle the substantial amount of data involved in seismic processing.

3.1 Quantitative Results

3.1.1 Experimental Setup and Data

For the demultiple task a synthetic common depth point (CDP) sorted dataset is used. The seismic input gathers consist of the merged primaries and multiples, and the corresponding labels consist only of the primaries. Each gather has a size of 64×512 samples and the dataset consists of 100,000 gathers. The synthetic seismic data was generated using the convolutional modeling as described in Fernandez et al. [2025].

For the interpolation and denoising tasks, we use the open source 2007 BP Anisotropic Velocity Benchmark [Shah, 2007] dataset, consisting of 1641 shot gathers of size 800×1151 . Due to the prominence of the first break and the extensive empty sections above it in the 2007 BP Anisotropic Velocity Benchmark, random cuts of the size 224×224 are applied below the first break. This is done, in order to ensure that each gather contains meaningful seismic information.

For all three applications a random sign change with a 50% chance of occurring is applied. Furthermore, for interpolation and denoising 50% of the time the gather is flipped horizontally. While the additive inversion and horizontal flips are applied after the z-scoring and normalizing, random noise is added before. The added random noise is independently sampled for each gather and defined by its maximum strength, rate of occurrence and distribution. For interpolation and demultiple similar noise is added, with a maximum strength of 25% of the maximum absolute value of the gather, a 50% rate of occurrence and a uniform distribution. This noise is added to the input as well as to the labels. In contrast, the noise for denoising is only applied to the input data. Its maximum strength is 50% of the maximum absolute amplitude of the gather, it is always applied and stems from a Gaussian distribution.

Additionally, the gathers are z-scored per gather and then normalized between -1 and 1 . This is done to match the value ranges of the seismic data to the natural image ones used during pre-training.

3.1.2 Impact of natural image pre-training

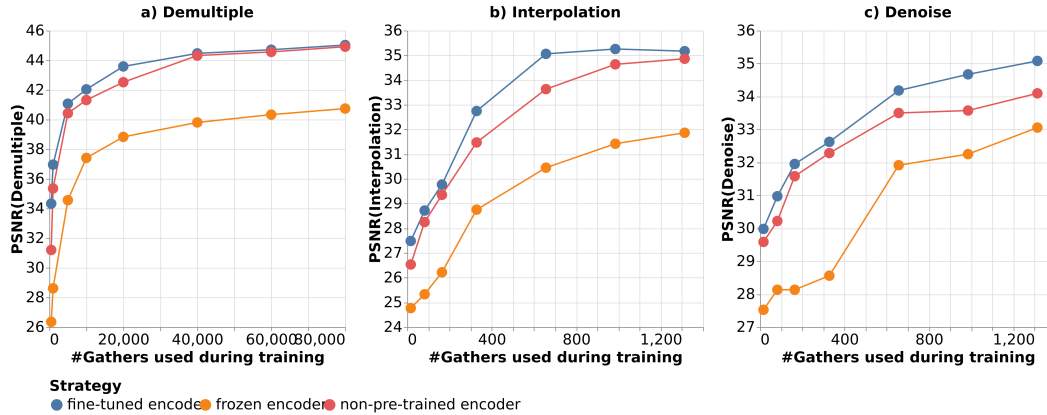


Figure 4: A comparison of the downstream training strategies for the Swin model family. Each plot in the figure depicts the PSNR achieved by the Swin model trained with the three distinct training strategies on a growing downstream task dataset for a specific downstream task. Plot a) shows the results for the demultiple task, plot b) for the interpolation task and plot c) for the denoising task. The observed ranking of these downstream training strategies is $fine\text{-tuned}\ encoder \geq non\text{-pre-trained}\ encoder \geq frozen\ encoder$, independently of the downstream task and dataset size.

Figure 4 presents a comparison of the downstream training strategies, outlined in the 2.2 section, for the Swin model family. The Swin model family was chosen, because it is the best performing model across all three tasks, that we tested, as we will show in the following section. Each plot in the figure depicts the PSNR achieved by the Swin model trained with the three distinct training strategies on a growing downstream task dataset. From left to right, the plots show the results for the demultiple, interpolation and denoising task. The observed ranking of these downstream training strategies is $fine\text{-tuned}\ encoder \geq non\text{-pre-trained}\ encoder \geq frozen\ encoder$, independently of the downstream task and dataset size. This demonstrates that pre-training on natural images is always comparable to or superior to random initialization. The latter holds particularly for lower data regimes, but even for larger datasets, such as the demultiple dataset. This suggests that during natural image pre-training, the model may develop capabilities that extend beyond those learnable from the specific downstream task.

Furthermore, the figure demonstrates the validity of our assumption, that the performance of the strategy $frozen\ encoder$ is correlated with that of the other two strategies. Consequently, it can be

inferred that better performance using the strategy *frozen encoder* should be reflected by improved performance using the other two strategies. Therefore, the results in the subsequent sections are from models trained with the strategy *frozen encoder*, except for our baselines. This is because the strategy *frozen encoder*, while performing worse than the other two, is significantly cheaper to compute. As baselines, we employed a Swin and a ConvNeXt model (both in their V1 variant) trained with strategy *non-pre-trained encoder*, which is the dominant strategy used in seismic processing.

3.1.3 Impact of the FM Architecture

Figure 5 presents three graphs, which plot the PSNR for the different seismic processing tasks against each other. While only the PSNR is displayed here, the structural similarity index measure (SSIM) and mean squared error (MSE) were also recorded, but not included in the plots as they are highly correlated with the PSNR, as evidenced in Appendix A.1. The legend encompasses the backbone archetype and the pre-training strategy. The former pertains to a model family, for instance, all ConvNeXt models are under the CONVNEXT archetype, irrespective of the pre-training strategy and version (V1 and V2). Furthermore, all model sizes (TINY, SMALL, BASE) fall under the same archetype, as seen later in Figure 10. The latter were introduced earlier. The only addition is NO_PRE_TRAINING which indicates that the model was trained end-to-end for this specific downstream task without a pre-trained encoder (strategy *non-pre-trained encoder*). These models serve as a baseline for comparison. All other models were trained using strategy *frozen encoder*.

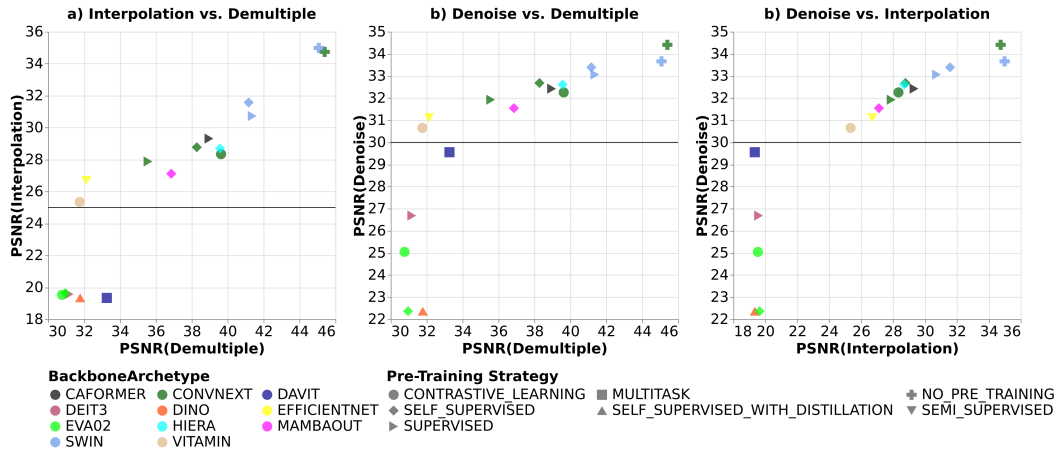


Figure 5: Comparison of different FMs on the various seismic processing tasks. Each plot contrasts the PSNR of two downstream tasks. Plot a) shows the results for the interpolation task contrasted against the demultiple task, plot b) for the denoising task against the demultiple task and plot c) for the denoising task against the interpolation task. The horizontal lines delineate the PSNRs of the hierarchical and non-hierarchical models to demonstrate the performance gap between them. Swin models perform the best across all three tasks, followed by Hiera, CAFormer and ConvNeXt depending on the downstream task.

As indicated above, the results demonstrate that non-hierarchical models perform significantly worse than their hierarchical counterparts. To visually emphasize this discrepancy, horizontal lines have been drawn in Figure 5, delineating the PSNRs of these two model types. The exception to that, are the models ViTamin and EfficientNet on the demultiple task, where they perform significantly worse than the other hierarchical models and similar to the non-hierarchical models, with Dual Attention Vision Transformer (DaViT) even outperforming them. Otherwise, the best performance of a non-hierarchical model is again DaViT this time for denoising, where it is significantly better than the other non-hierarchical models, but still achieved a PSNR of 1.1 dB less than the worst hierarchical model achieved.

Overall the best performing models are Swin models, followed by Hiera, CAFormer or ConvNeXt models depending on the downstream task. While for demultiple and interpolation there is a significant gap between them and our baselines the gap narrows for denoising, especially when only considering the Swin models. Interestingly, while the Swin archetype always outperforms the

ConvNeXt archetype, the ConvNeXt baseline is slightly better in demultiple and denoising than the Swin baseline. This may indicate that the Swin models learn more generalizable image features during pre-training and lend itself better to transfer learning.

3.1.4 Pre-Training Strategy and Downstream Task Correlation

Interestingly, in our findings the optimal pre-training strategies differ between tasks. The interpolation and denoising tasks both perform better with self-supervised pre-training when available, as is the case with Swin and ConvNeXt models. Demultiple, conversely, performs better with supervised or contrastive pre-training for Swin and ConvNeXt respectively. One thing to keep in mind, is that while the dataset for self-supervised and supervised pre-training was the same, the dataset for contrastive pre-training was significantly bigger, as we will show in following section.

Downstream task performance is highly correlated especially for the hierarchical models, which is also similar to the findings of Goldblum et al. [2023]. The specific Pearson’s correlations are shown in Appendix A.1. While the non-hierarchical models perform similarly for interpolation, there is a small difference between the results for demultiple and a significant difference between the results for denoising. This correlation between downstream tasks also supports the creation of an SFM, because an SFM should collectively maximize its performance on all downstream tasks.

3.1.5 Combined Downstream Task Performance

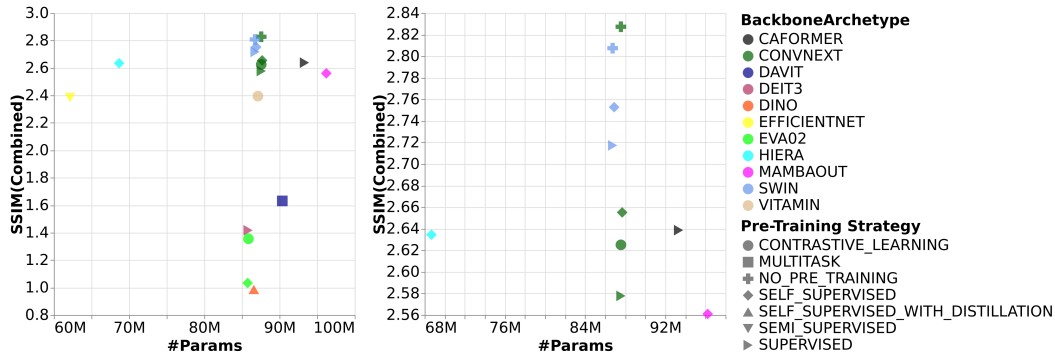


Figure 6: Comparison of the combined performance of the different FMs contrasted against their number of parameters. The left plot shows all the tested FMs and the right plot only the FMs with a combined SSIM above 2.5 to further highlight the difference between the well performing models. The well performing models are Swin, ConvNeXt, Hiera, CAFormer and MambaOut. While most of the well performing models have a similar number of parameters Hiera is significantly smaller.

After looking at the individual results by downstream tasks, Figure 6 shows the combined SSIM ($SSIM_{combined} = SSIM_{Demultiple} + SSIM_{Interpolation} + SSIM_{Denoise}$) for each model against the parameters of the FM used as the image encoder. For the combined score the SSIM was chosen, because it has a known upper bound of one, which not only equally weights the different downstream tasks but also gives us a theoretical upper bound of performance. On the left, all different tested models are displayed and on the right, only models which have a combined SSIM above 2.5 are displayed. This removes all non-hierarchical models, as well as EfficientNet and ViTamin. The best overall model is Swin (V2) pre-trained via self-supervision, followed by Swin (V1) pre-trained via supervision. The third-best model is ConvNeXt (V2) pre-trained via self-supervision. The fourth-best model is CAFormer closely followed by Hiera. Interestingly, CAFormer is performing that well despite being trained via supervision. While the optimal training strategy is task dependent, as mentioned above, across all three downstream tasks self-supervision seems to perform better if available. This could mean, that pre-training CAFormer via self-supervision could improve results significantly, maybe even beyond ConvNeXt (V2).

3.1.6 Impact of the Pre-Training Dataset

Figure 7 shows that not only the pre-training strategy, but also the dataset and its size, differs. As in Figure 6, all tested models are displayed on the left, and only the ones with a combined SSIM above 2.5 on the right. In addition, the x-axis of the right plot has a logarithmic scale to better highlight the differences for the smaller datasets, which are otherwise lost with a linear scale. Even though some of the non-hierarchical models were trained on vast datasets, architecture seems to play a more critical role for seismic processing tasks. Nevertheless, even among the hierarchical models there are significant differences in the pre-training dataset sizes that could affect the results. While Swin outperforms ConvNeXt it was also pre-trained on a larger dataset (ImageNet-22k vs. ImageNet-1k) than the other models. The exception are HierA and the ConvNeXt pre-trained via contrastive learning, both were pre-trained on a significantly larger dataset than the Swin models. More interesting for an SFM, however, is that even models pre-trained on small pre-training datasets yielded good results.

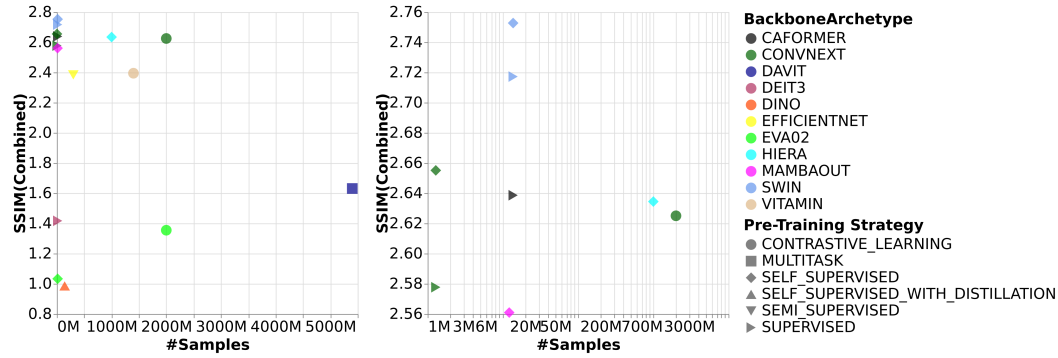


Figure 7: Comparison of the combined performance of the different FMs contrasted against the size of the pre-training dataset. The left plot shows all the tested FMs and the right one only the FMs with a combined SSIM above 2.5 to further highlight the difference between the well performing models. Additionally, the right plot uses a log scaling for the x-axis to demonstrate the differences between the smaller datasets, which vanish with the linear scale. The well performing models are Swin, ConvNeXt, HierA, CAFormer and MambaOut. Of these HierA and MambaOut were trained on a significantly larger dataset and ConvNeXt on the smallest.

3.1.7 Impact of Model Size and Inference Time

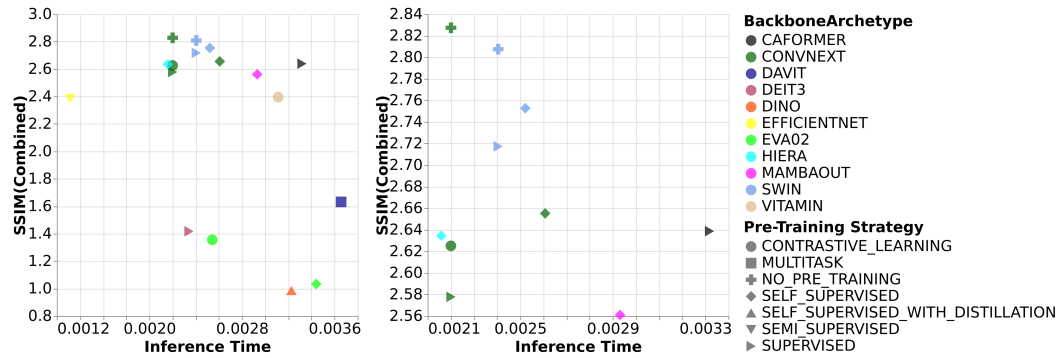


Figure 8: Comparison of the combined performance of the different FMs contrasted against their inference time. The left plot shows all the tested FMs and the right one only the FMs with a combined SSIM above 2.5 to further highlight the difference between the well performing models. The well performing models are Swin, ConvNeXt, HierA, CAFormer and MambaOut. Interestingly, the V2 versions of Swin and ConvNeXt are slower than their V1 counterparts. Additionally, CAFormer is significantly slower than the other tested FMs.

While only the base model versions are compared in this section, and therefore the number of parameters are similar, two exceptions are EfficientNet and Hiera, which are significantly smaller, see Figure 6. While for EfficientNet this also results in a faster inference time, this is not the case for Hiera, which is only slightly faster than ConvNeXt despite having significantly fewer parameters, as can be seen in Figure 8. Another interesting fact, is that for both ConvNeXt and Swin the V2 versions, which have only minimal architectural changes to accommodate self-supervised pre-training, are slower than their V1 counterparts. The inference times were measured on an A100 using the implementations of Wightman [2019] without torch.compile, a batch size of 512 and gathers of size 224x224. The applicability of these larger FMs is shown by the Swin (V2) inference time of about 2.5 ms, which translates into around 400 gathers per second. Especially considering, that these inference results are without any optimizations or quantization, which could potentially speed up the model drastically.

3.1.8 Impact of Embedding Space Size

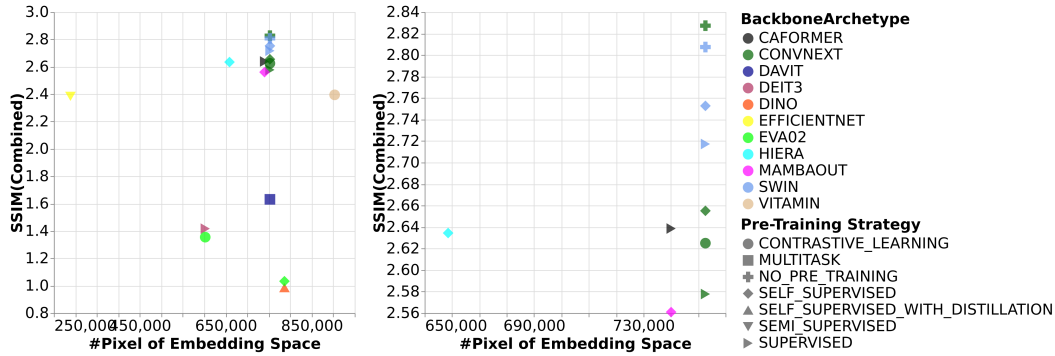


Figure 9: Comparison of the combined performance of the different FMs contrasted against the size of their embedding space. The left plot shows all the tested FMs and the right one only the FMs with a combined SSIM above 2.5 to further highlight the difference between the well performing models. The well performing models are Swin, ConvNeXt, Hiera, CAFormer and MambaOut. While most of the well performing models have a similar sized embedding space the embedding space of Hiera is significantly smaller.

The final criterion we used to compare these models is the number of pixels in the embedding space, as illustrated in Figure 9. The embedding space $\{E_s : E_s \in \mathbb{R}^{C_s \times H_s \times W_s} \quad \forall \quad 1 \leq s \leq S\}$ is the output of the encoder, as defined in Equation (2). The number of pixels then is the sum over the sizes of each embedding $(\sum_{s=1}^S C_s \times H_s \times W_s)$. Focusing on the right graph, which again shows only the model with a combined SSIM above 2.5, we can see that the Swin and ConvNeXt models have the same number of pixels. This is by design, as their channel size was chosen to match a ViT and their down-scaling between stages is identically. However, Hiera has a significantly smaller number of pixels for the same down-scaling factors. This could indicate that smaller channel sizes and therefore smaller models could still lead to good results.

3.1.9 Impact of Model Scaling

In order to ascertain, whether smaller models can still perform well, we compare different model sizes for four archetypes, namely CAFormer, ConvNeXt (V2), Hiera and Swin (V1) on all three seismic processing tasks, see Figure 10. These archetypes were selected because they performed the best across the three tested downstream tasks. For Swin the V1 variant was chosen instead of the V2 variant, because it was available pre-trained in more different model sizes. We opted for the PSNR as the metric instead of the SSIM, as it offers a broader domain, making differentiation between the results of the different models easier.

The left plot displays the results for the demultiple task and again confirms our earlier results regarding the ranking for the base model size (around 100M parameters) of Swin > Hiera > CAFormer > ConvNeXt. However, the ranking changes for smaller and larger models, where Hiera outperforms

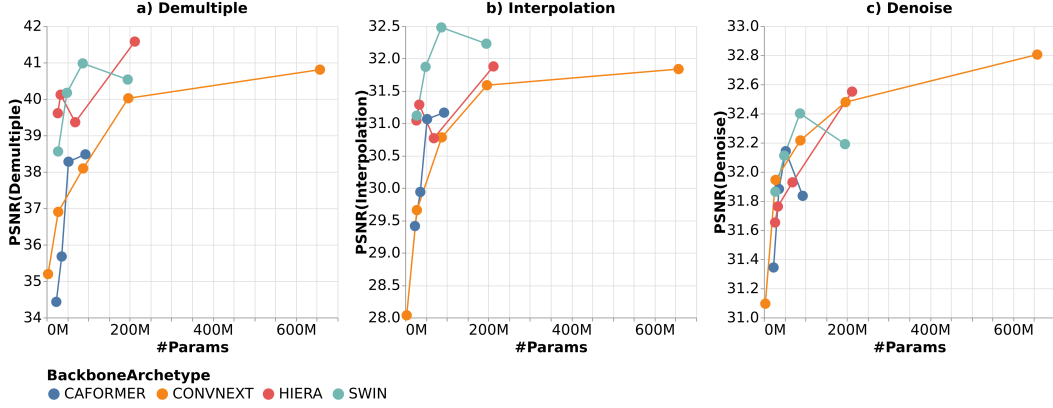


Figure 10: Performance comparison with scaling model size for the four top performing backbone archetypes on each different downstream task. Plot a) shows the results for the demultiple task, plot b) for the interpolation task and plot c) for the denoising task. As can be seen, smaller HierA or Swin models still perform well, especially for demultiple and interpolation, where they perform better than significantly larger ConvNeXt models. Additionally, the largest Swin seems to be over-fitted on the pre-training data. The base HierA performs worse than expected for demultiple and interpolation, but further testing showed that these results are not outliers.

the Swin models. The drop in performance of the HierA BASE_PLUS version is confounding, but the experiment was repeated an additional five times, even changing the learning rate slightly, and achieved a mean PSNR of 38.96 with an std of 0.46, which shows that the original value of 39.36 was actually a positive outlier. The results for denoising, plotted on the right, also show that the drop in performance is task dependent, because for denoising HierA scales as expected. For interpolation the performance of HierA BASE_PLUS drops again compared to its smaller and larger counterparts, but in contrast to the demultiple results, the Swin models outperform the HierA models at all scales. The Swin LARGE model appears to be overfitted on the pre-training dataset. However, the smaller Swin models demonstrate notable efficacy, outperforming significantly larger ConvNeXt models. Another outlier is the result of the CAFormer B36 model on denoising, where it exhibits inferior performance compared to its smaller counterparts, despite slightly outperforming them in the other two downstream tasks. To ensure the reliability of these findings, the experiment was repeated five additional times, resulting in an average score of 31.9 with a standard deviation of 0.14. While our initial result was slightly worse than the mean performance it remained within expected margins. In conclusion, the findings suggest that smaller HierA or Swin models could be interesting candidates for a more efficient SFM.

3.2 Qualitative Results

This section presents qualitative results following the quantitative results in the preceding section. To ensure conciseness, solely the results of the two baseline models (ConvNeXt (A) and Swin (B)) and the overall best non-baseline model (Swin V2 (C)) are displayed. Each of these three models was trained specially for each task, resulting in a total of nine distinct models. Importantly, the following qualitative results are presented to contextualize the quantitative metrics, not to claim improvements over the current state of the art.

3.2.1 Interpolation

Figure 11 depicts the PSNRs of the three models for the interpolation task. The input data for this task is a gather from the evaluation set, which was not observed during training. The first row, consist of this gather G and the decimated gather $D(G)$. The subsequent rows consist of the predicted gather G^* and the residual $R = (G - G^*) \times 10$ of each model. While the predicted gathers (P^*) appear similar, the differences become more apparent when observing the residual (R). While the results of baseline (A) and baseline (B) are similar, the results of model (C) differ significantly. This is confirmed by the calculated PSNRs, which are 39.24 for (B), 38.05 for (A) and only 34.96 for (C).

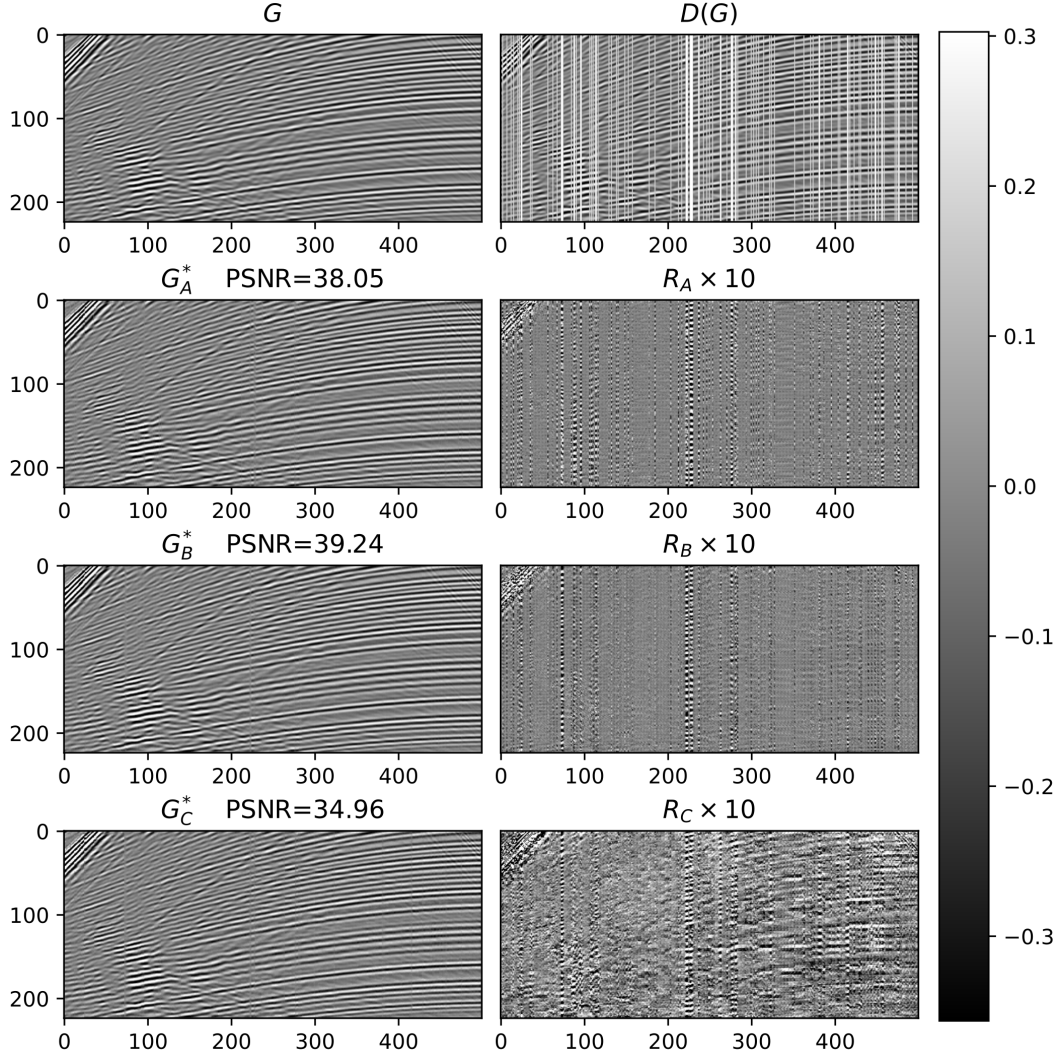


Figure 11: Interpolation results of the two baselines (ConvNeXt (A) and Swin (B)) and the best overall model trained with strategy *frozen encoder* (Swin V2 (C)) on a gather from the evaluation set. For each model the predicted gather G^* as well as the residual $R = G - G^*$ is displayed.

Nonetheless, the results of (C) are impressive considering, that the encoder and therefore the majority of the model (in this case 91% of the total parameters), was trained exclusively on natural images.

3.2.2 Denoising

Figure 12 depicts the results of the three models for the denoising task. Similar to the interpolation task, a gather from the evaluation set, is used as input. But to better test the generalization ability of these models, uniform noise is added, instead of the Gaussian noise, that was added during training. The first row, consist of a gather G , as well as the gather $G + N$. The other rows consist of the predicted gather G^* and the predicted noise $N^* = (G + N) - G^*$ of each model. This time the predicted gathers (P^*), as well as the predicted noise N^* appear similar, across all three models. This is further corroborated by the calculated PSNRs, which are 28.74 for (B), 27.67 for (A) and 27.45 for (C). Impressively, the results of (C) are of comparable quality to the baseline, especially considering again, that the encoder has not seen any seismic data.

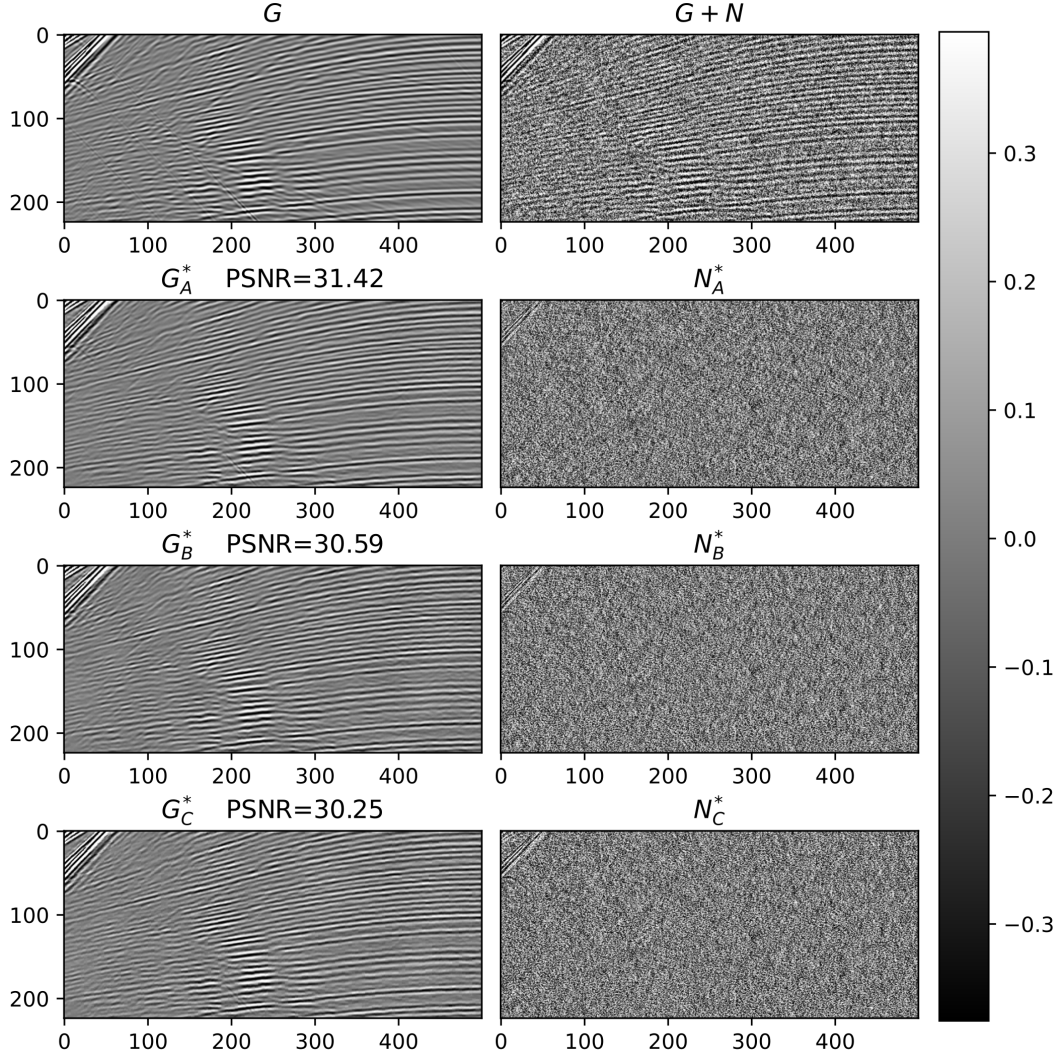


Figure 12: Denoising results of the two baselines (ConvNeXt (A) and Swin (B)) and the best overall model trained with strategy *frozen encoder* (Swin V2 (C)) on a gather from the evaluation set. For each model the predicted gather G^* as well as the predicted noise $N^* = (G + N) - G^*$ is displayed.

3.2.3 Demultiple

Figure 13 presents the results of these models for the demultiple task on a gather from a post-migration dataset from the North Sea Volve field. The first image is the input gather containing primaries (P) and multiples (M). The second, third and fourth image depict the predicted primaries (P^*) by each model. The last three images correspond to the predicted multiples ($M^* = (M + P) - P^*$), which are derived by subtraction of the predicted primaries from the input gather.

While the predicted primaries (P^*) appear similar, the differences become more evident when observing the predicted multiples (M^*). The primary dissimilarities of these are in the top third, influenced by the mute and first break. Interestingly, the results from baseline (B) and the overall best model (C) resemble each other more than the results of the two baselines. This indicates that the architecture seems to be more influential than the training strategy when it comes to handling the mute and the first break. The results of (C) are particularly noteworthy, considering that only the decoder was trained on seismic data.

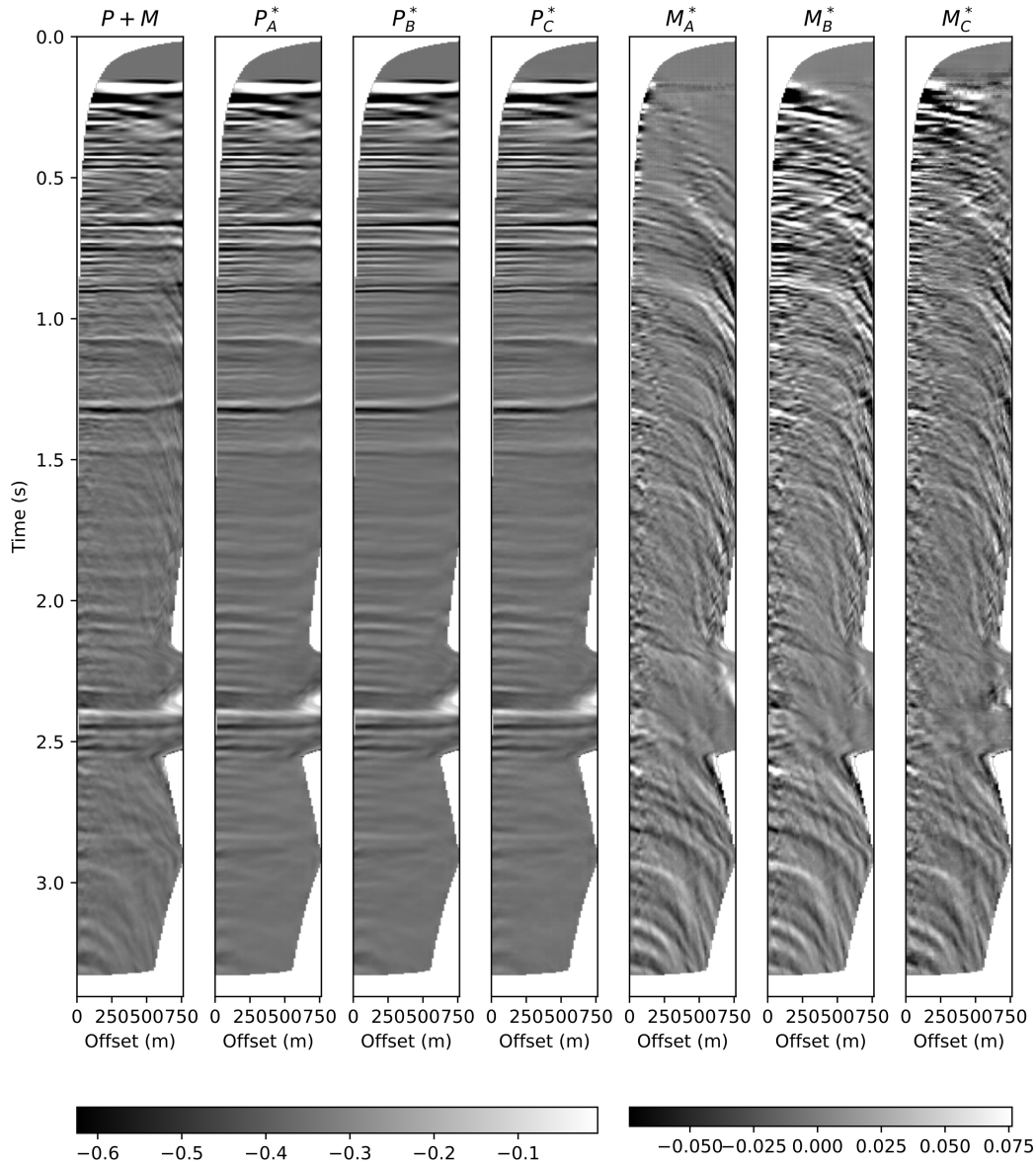


Figure 13: Demultiple results of the two baselines (ConvNeXt (A) and Swin (B)) and the best overall model trained with strategy *frozen encoder* (Swin V2 (C)) on the North Sea Volve field data. For each model the predicted primaries (P^*) and the predicted multiples (M^*) are displayed.

4 Discussion

In this section, we will explore several significant findings from our study. We will begin with the significance of hierarchical models, followed by the influence and importance of pre-training methods. Finally, we will address the issues of generalization and the performance of various downstream training strategies.

4.1 Importance of hierarchical models

The most critical finding in this paper is arguably the discrepancy in performance between hierarchical and non-hierarchical models. This finding is corroborated by Goldblum et al. [2023], yet the majority of the FMs in the seismic space utilize a non-hierarchical model, as seen in Sheng et al. [2024], Sansal et al. [2025] and Pham et al. [2025], all of whom employ a ViT. It should be noted, that the results of this investigation are likely more pronounced due to the fact that all the downstream tasks are pixel-level regression tasks. The discrepancy between hierarchical and non-hierarchical models is likely diminished for downstream tasks that do not necessitate pixel level precision, such as classification and segmentation. Nonetheless, we believe that hierarchical models should still exhibit superior performance in these tasks, as indicated by Goldblum et al. [2023], who showed that Swin outperforms ViT in some natural image tasks.

This hypothesis is further substantiated by the observation that the discrepancy between hierarchical and non-hierarchical models is smallest for the denoising task. This can be attributed to the fact that denoising relies less heavily on the higher scale features available through hierarchical models compared to the other two downstream tasks. Noise, being high frequency content, is predominantly present in the higher scale features. Nevertheless, hierarchical models still provide a significant performance gain for denoising, as shown in Figure 5.

Also, the discrepancy between the results of the *frozen-encoder* strategy and those of the other two is the least significant for denoising, as shown in Figure 4 and Figure 12. This could be attributed to the inherent Gaussian noise in natural images, which the encoder learns through self-supervision without being explicitly trained on denoising.

4.2 Pre-training strategies and their relevance for an SFM

Another finding less relevant for training an SFM but more interesting from a transfer learning perspective, is that the optimal pre-training strategy differs between downstream tasks. While the reason why self-supervision as pre-training strategy is more optimal for interpolation is clear due to the similarity between both tasks, the reasoning behind the optimal choice for the other two downstream tasks is less clear. These results are similar to those of Goldblum et al. [2023], who showed that the optimal pre-training strategy also differs for natural image tasks. The analysis of pre-training strategies is impeded by the lack of isolated comparison between them. Most pre-training strategies are only available for one model and one dataset. A more fair comparison would be interesting, but would need to be done in the natural image domain. This is because some of the pre-training strategies require a language mapping which is infeasible for seismic data. Additionally, most pre-training strategies require labeled data which is also infeasible for seismic data. Therefore, the only applicable pre-training strategy without synthetic data, for an SFM is self-supervision. Relying on synthetic data semi-supervised learning could also be an alternative, as shown by Cheng et al. [2025].

A notable benefit of self-supervised pre-training on seismic data is its capacity to learn features directly from the data itself. This approach stands in contrast, to the prevailing strategy of training on synthetic data and attempting to enhance it to improve generalization on real data. While Figure 4 demonstrates the comparable or superior performance of fine-tuning a natural image pre-trained model compared to only training on synthetic data, we hypothesize that pre-training on seismic data will yield even better results. A subject that merits further exploration is whether it is preferable to train smaller, more efficient models for significantly different regions or to train a single, large model on all available data.

4.3 Baseline Performance and Generalization

While the transfer performance of ConvNeXt trained with strategy *frozen encoder* was significantly worse than Swin, especially when considering different model sizes, the qualitative results for interpolation and denoising showed that the baseline ConvNeXt model that was trained using strategy *non-pre-trained encoder* was similar in quality if not better than the Swin baseline. We hypothesize that this is due to these examples aligning closely to the training distribution and that Swin models generalize better. This is based on the quantitative results of these models trained with strategy *frozen encoder* and further corroborated by the qualitative results for demultiple on the North Sea Volve field data.

On the topic of out of distribution generalization, we theorize that the training data used for interpolation and denoising while large enough for in distribution generalization is too small for out of distribution generalization. Therefore, the qualitative results for these two task are shown for in distribution examples. While the interpolation example is completely in distribution, the denoise example is shifted a bit outside distribution by changing the noise distribution but not the underlying seismic distribution. In contrast, the qualitative example for demultiple is from the North Sea Volve field data and therefore out of distribution. Nonetheless, the results are impressive which is in part due to the synthetic training data, which was generated with the explicit intent of wide generalization.

5 Conclusion

We conducted a comprehensive investigation into various FMs and developed a framework for further testing. Our main focus was on seismic processing, evaluating the performance of the different FMs on three seismic processing tasks: demultiple, interpolation, and denoising. We quantitatively evaluated a diverse range of FMs using synthetic data, aiming to clarify how various model characteristics, such as pre-training techniques and architectural design choices, affect their performance. Additionally, we selected a subset of models for qualitative assessment and presented the demultiple results of real field data. In our comparison of different FMs we also examined the effects of natural image pre-training, with and without additional fine-tuning.

In summary, finding the optimal architecture for seismic processing presents a difficult and multifaceted challenge. However, our research has yielded to some key findings. Firstly, that future SFM, especially if they are intended for seismic processing tasks, should use hierarchical models rather than non-hierarchical ones. Secondly, that Swin seems to be the best overall for models larger than 50M parameters, while Hiera may be an alternative option for smaller models. Thirdly, that pre-training, even on natural images, consistently performs as well as or better than no pre-training for all data regimes. Finally, the performance of seismic processing tasks is highly correlated, which supports the creation of an SFM for processing tasks, because a SFMs should collectively maximize its performance on all downstream tasks.

6 Data Availability Statement

The training data for the interpolation and denoise task is the 2007 BP Anisotropic Velocity Benchmark dataset [Shah, 2007]. It is an open seismic dataset created by Hemang Shah and provided by BP Exploration Operation Company Limited ("BP"). It can be obtained by visiting https://wiki.seg.org/wiki/2007_BP_Anisotropic_Velocity_Benchmark. Additionally, the North Sea Volve dataset was used for the qualitative demultiple results. It is also an open seismic dataset and can be obtained by visiting <https://www.equinor.com/energy/volvedata-sharing>.

Acronyms

DL deep learning	1
FM foundation model	2
SFM seismic foundation model	2
ViT Vision Transformer	2
Swin Swin Transformer	2
DaViT Dual Attention Vision Transformer	10
PSNR peak signal-to-noise ratio	
SSIM structural similarity index measure	10
MSE mean squared error	10
BERT Bidirectional Encoder Representations from Transformers	2
MAE masked autoencoders	2
GSFM generative seismic foundation model	3
MIM Masked Image Modeling	5
CNN convolutional neural network	5
CV computer vision	1

References

- Özdoğan Yilmaz and Stephen M. Doherty. *Seismic Data Analysis: Processing, Inversion, and Interpretation of Seismic Data*. SEG Books, 2001. ISBN 978-1-56080-094-1.
- Daniel Trad, Tadeusz Ulrych, and Mauricio Sacchi. Latest views of the sparse Radon transform. *GEOPHYSICS*, 68(1):386–399, January 2003. ISSN 0016-8033. doi:10.1190/1.1543224.
- S. Mostafa Mousavi and Gregory C. Beroza. Deep-learning seismology. *Science*, 377(6607): eabm4470, August 2022. doi:10.1126/science.abm4470.
- Xintao Chai, Hanming Gu, Feng Li, Hongyou Duan, Xiaobo Hu, and Kai Lin. Deep learning for irregularly and regularly missing data reconstruction. *Scientific Reports*, 10(1):3302, February 2020. ISSN 2045-2322. doi:10.1038/s41598-020-59801-x.
- M. Fernandez, R. Durall, N. Ettrich, M. Delescluse, A. Rabaute, and J. Keuper. A BENCHMARK STUDY OF DEEP LEARNING METHODS FOR SEISMIC INTERPOLATION. *83rd EAGE Conference and Exhibition 2022*, 4(1):2674–2678, June 2022a. doi:10.3997/2214-4609.202210725/CITE/REFWORKS.
- M. Fernandez, R. Durall, N. Ettrich, M. Delescluse, A. Rabaute, and J. Keuper. A comparison of deep learning paradigms for seismic data interpolation. In *Second EAGE Digitalization Conference and Exhibition*, volume 2022, pages 1–5. European Association of Geoscientists & Engineers, March 2022b. doi:10.3997/2214-4609.202239028.

- Sara Mandelli, Vincenzo Lipari, Paolo Bestagini, and Stefano Tubaro. Interpolation and Denoising of Seismic Data using Convolutional Neural Networks, October 2019.
- Claire Birnie, Matteo Ravasi, Sixiu Liu, and Tariq Alkhalifah. The potential of self-supervised networks for random noise suppression in seismic data. *Artificial Intelligence in Geosciences*, 2: 47–59, December 2021. ISSN 2666-5441. doi:10.1016/j.aiig.2021.11.001.
- Chenyu Qiu, Bangyu Wu, Naihao Liu, Xu Zhu, and Haoran Ren. Deep Learning Prior Model for Unsupervised Seismic Data Random Noise Attenuation. *IEEE Geoscience and Remote Sensing Letters*, 19:1–5, 2022. ISSN 1558-0571. doi:10.1109/LGRS.2021.3053760.
- Mi Zhang, Yang Liu, and Yangkang Chen. Unsupervised Seismic Random Noise Attenuation Based on Deep Convolutional Neural Network. *IEEE Access*, 7:179810–179822, 2019. ISSN 2169-3536. doi:10.1109/ACCESS.2019.2959238.
- Shirui Wang, Wenyi Hu, Pengyu Yuan, Xuqing Wu, Qunshan Zhang, Prashanth Nadukandi, German Ocampo Botero, and Jiefu Chen. Seismic debrending by self-supervised deep learning with a blind-trace network. In *First International Meeting for Applied Geoscience & Energy Expanded Abstracts*, SEG Technical Program Expanded Abstracts, pages 3194–3198. Society of Exploration Geophysicists, September 2021a. doi:10.1190/segam2021-3583662.1.
- Rui Guo, Hiren Maniar, Haibin Di, Nick Moldoveanu, Aria Abubakar, and Maokun Li. Ground roll attenuation with an unsupervised deep learning approach. In *SEG Technical Program Expanded Abstracts 2020*, SEG Technical Program Expanded Abstracts, pages 3164–3168. Society of Exploration Geophysicists, September 2020. doi:10.1190/segam2020-3425792.1.
- Harpreet Kaur, Sergey Fomel, and Nam Pham. Seismic ground-roll noise attenuation using deep learning. *Geophysical Prospecting*, 68(7):2064–2077, 2020. ISSN 1365-2478. doi:10.1111/1365-2478.12985.
- Wenlong Wang, George A. McMechan, Jianwei Ma, and Fei Xie. Automatic velocity picking from semblances with a new deep-learning regression strategy: Comparison with a classification approach. *GEOPHYSICS*, 86(2):U1–U13, March 2021b. ISSN 0016-8033. doi:10.1190/geo2020-0423.1.
- Danilo Chamorro, Jiahua Zhao, Claire Birnie, Myrna Staring, Moritz Fliedner, and Matteo Ravasi. Deep learning-based extraction of surface wave dispersion curves from seismic shot gathers. *Near Surface Geophysics*, 22(4):421–437, 2024. ISSN 1873-0604. doi:10.1002/nsg.12298.
- Tom Brown, Benjamin Mann, Nick Ryder, Melanie Subbiah, Jared D Kaplan, Prafulla Dhariwal, Arvind Neelakantan, Pranav Shyam, Girish Sastry, Amanda Askell, Sandhini Agarwal, Ariel Herbert-Voss, Gretchen Krueger, Tom Henighan, Rewon Child, Aditya Ramesh, Daniel Ziegler, Jeffrey Wu, Clemens Winter, Chris Hesse, Mark Chen, Eric Sigler, Mateusz Litwin, Scott Gray, Benjamin Chess, Jack Clark, Christopher Berner, Sam McCandlish, Alec Radford, Ilya Sutskever, and Dario Amodei. Language Models are Few-Shot Learners. In *Advances in Neural Information Processing Systems*, volume 33, pages 1877–1901. Curran Associates, Inc., 2020.
- Alexander Kirillov, Eric Mintun, Nikhila Ravi, Hanzi Mao, Chloe Rolland, Laura Gustafson, Tete Xiao, Spencer Whitehead, Alexander C. Berg, Wan-Yen Lo, Piotr Dollár, and Ross Girshick. Segment Anything, April 2023.
- Robin Rombach, Andreas Blattmann, Dominik Lorenz, Patrick Esser, and Björn Ommer. High-Resolution Image Synthesis with Latent Diffusion Models, April 2022.
- Yixin Liu, Kai Zhang, Yuan Li, Zhiling Yan, Chujie Gao, Ruoxi Chen, Zhengqing Yuan, Yue Huang, Hanchi Sun, Jianfeng Gao, Lifang He, and Lichao Sun. Sora: A Review on Background, Technology, Limitations, and Opportunities of Large Vision Models, April 2024.
- Alexey Dosovitskiy, Lucas Beyer, Alexander Kolesnikov, Dirk Weissenborn, Xiaohua Zhai, Thomas Unterthiner, Mostafa Dehghani, Matthias Minderer, Georg Heigold, Sylvain Gelly, Jakob Uszkoreit, and Neil Houlsby. An Image is Worth 16x16 Words: Transformers for Image Recognition at Scale, October 2020.

- Zhuang Liu, Hanzi Mao, Chao-Yuan Wu, Christoph Feichtenhofer, Trevor Darrell, and Saining Xie. A ConvNet for the 2020s, March 2022a.
- Ze Liu, Yutong Lin, Yue Cao, Han Hu, Yixuan Wei, Zheng Zhang, Stephen Lin, and Baining Guo. Swin Transformer: Hierarchical Vision Transformer using Shifted Windows, August 2021.
- Randy Harsuko and Tariq Alkhalifah. StorSeismic: A new paradigm in deep learning for seismic processing. *IEEE Transactions on Geoscience and Remote Sensing*, 60:1–15, 2022. ISSN 0196-2892, 1558-0644. doi:10.1109/TGRS.2022.3216660.
- Jacob Devlin, Ming-Wei Chang, Kenton Lee, and Kristina Toutanova. BERT: Pre-training of Deep Bidirectional Transformers for Language Understanding, May 2019.
- Hanlin Sheng, Xinming Wu, Xu Si, Jintao Li, Sibozhang, and Xudong Duan. Seismic Foundation Model (SFM): A next generation deep learning model in geophysics. *GEOPHYSICS*, pages 1–64, December 2024. ISSN 0016-8033. doi:10.1190/geo2024-0262.1.
- Nam Pham, Haibin Di, Tao Zhao, and Aria Abubakar. SeisBERT: A pretrained seismic image representation model for seismic data interpretation. *The Leading Edge*, 44(2):96–106, February 2025. ISSN 1070-485X. doi:10.1190/tle44020096.1.
- Altay Sansal, Ben Lasscock, and Alejandro Valenciano. Scaling Seismic Foundation Models. *First Break*, 43(2):69–74, February 2025. ISSN 0263-5046, 1365-2397. doi:10.3997/1365-2397.fb2025016.
- Kaiming He, Xinlei Chen, Saining Xie, Yanghao Li, Piotr Dollár, and Ross Girshick. Masked Autoencoders Are Scalable Vision Learners, November 2021.
- Shijun Cheng, Randy Harsuko, and Tariq Alkhalifah. A generative foundation model for an all-in-one seismic processing framework, February 2025.
- Micah Goldblum, Hossein Souri, Renkun Ni, Manli Shu, Viraj Prabhu, Gowthami Somepalli, Prithvijit Chattopadhyay, Mark Ibrahim, Adrien Bardes, Judy Hoffman, Rama Chellappa, Andrew Gordon Wilson, and Tom Goldstein. Battle of the Backbones: A Large-Scale Comparison of Pretrained Models across Computer Vision Tasks, November 2023.
- Hang Zhao, Orazio Gallo, Iuri Frosio, and Jan Kautz. Loss Functions for Image Restoration With Neural Networks. *IEEE Transactions on Computational Imaging*, 3(1):47–57, March 2017. ISSN 2333-9403. doi:10.1109/TCI.2016.2644865.
- Olaf Ronneberger, Philipp Fischer, and Thomas Brox. U-Net: Convolutional Networks for Biomedical Image Segmentation, May 2015.
- Mario R. Fernandez, Norman Ertch, Matthias Delescluse, Alain Rabaute, and Janis Keuper. Towards deep learning for seismic demultiple. *Geophysical Prospecting*, n/a(n/a), 2025. ISSN 1365-2478. doi:10.1111/1365-2478.13672.
- Weihao Yu, Chenyang Si, Pan Zhou, Mi Luo, Yichen Zhou, Jiashi Feng, Shuicheng Yan, and Xinchao Wang. MetaFormer Baselines for Vision. *IEEE Transactions on Pattern Analysis and Machine Intelligence*, 46(2):896–912, February 2024. ISSN 1939-3539. doi:10.1109/TPAMI.2023.3329173.
- Sanghyun Woo, Shoubhik Debnath, Ronghang Hu, Xinlei Chen, Zhuang Liu, In So Kweon, and Saining Xie. ConvNeXt V2: Co-designing and Scaling ConvNets with Masked Autoencoders, January 2023.
- Mingyu Ding, Bin Xiao, Noel Codella, Ping Luo, Jingdong Wang, and Lu Yuan. DaViT: Dual Attention Vision Transformers, April 2022.
- Hugo Touvron, Matthieu Cord, and Hervé Jégou. DeiT III: Revenge of the ViT, April 2022.
- Maxime Oquab, Timothée Darcet, Théo Moutakanni, Huy Vo, Marc Szafraniec, Vasil Khalidov, Pierre Fernandez, Daniel Haziza, Francisco Massa, Alaaeldin El-Nouby, Mahmoud Assran, Nicolas Ballas, Wojciech Galuba, Russell Howes, Po-Yao Huang, Shang-Wen Li, Ishan Misra, Michael Rabbat, Vasu Sharma, Gabriel Synnaeve, Hu Xu, Hervé Jégou, Julien Mairal, Patrick Labatut, Armand Joulin, and Piotr Bojanowski. DINOv2: Learning Robust Visual Features without Supervision, February 2024.

- Mingxing Tan and Quoc V. Le. EfficientNet: Rethinking Model Scaling for Convolutional Neural Networks, September 2020.
- Yuxin Fang, Quan Sun, Xinggong Wang, Tiejun Huang, Xinlong Wang, and Yue Cao. EVA-02: A Visual Representation for Neon Genesis. *Image and Vision Computing*, 149:105171, September 2024. ISSN 02628856. doi:10.1016/j.imavis.2024.105171.
- Chaitanya Ryali, Yuan Ting Hu, Daniel Bolya, Chen Wei, Haoqi Fan, Po Yao Huang, Vaibhav Aggarwal, Arkabandhu Chowdhury, Omid Poursaeed, Judy Hoffman, Jitendra Malik, Yanghao Li, and Christoph Feichtenhofer. Hiera: A Hierarchical Vision Transformer without the Bells-and-Whistles. *Proceedings of Machine Learning Research*, 202:29441–29454, June 2023. ISSN 26403498.
- Weihao Yu and Xinchao Wang. MambaOut: Do We Really Need Mamba for Vision?, May 2024.
- Ze Liu, Han Hu, Yutong Lin, Zhuliang Yao, Zhenda Xie, Yixuan Wei, Jia Ning, Yue Cao, Zheng Zhang, Li Dong, Furu Wei, and Baining Guo. Swin Transformer V2: Scaling Up Capacity and Resolution, April 2022b.
- Jieneng Chen, Qihang Yu, Xiaohui Shen, Alan Yuille, and Liang-Chieh Chen. ViTamin: Designing Scalable Vision Models in the Vision-Language Era, April 2024.
- Olga Russakovsky, Jia Deng, Hao Su, Jonathan Krause, Sanjeev Satheesh, Sean Ma, Zhiheng Huang, Andrej Karpathy, Aditya Khosla, Michael Bernstein, Alexander C. Berg, and Li Fei-Fei. ImageNet Large Scale Visual Recognition Challenge, January 2015.
- Hangbo Bao, Li Dong, Songhao Piao, and Furu Wei. BEiT: BERT Pre-Training of Image Transformers, September 2022.
- Geoffrey Hinton, Oriol Vinyals, and Jeff Dean. Distilling the Knowledge in a Neural Network, March 2015.
- Qizhe Xie, Minh-Thang Luong, Eduard Hovy, and Quoc V. Le. Self-training with Noisy Student improves ImageNet classification, June 2020.
- Bin Xiao, Haiping Wu, Weijian Xu, Xiyang Dai, Houdong Hu, Yumao Lu, Michael Zeng, Ce Liu, and Lu Yuan. Florence-2: Advancing a Unified Representation for a Variety of Vision Tasks. In *2024 IEEE/CVF Conference on Computer Vision and Pattern Recognition (CVPR)*, pages 4818–4829, Seattle, WA, USA, June 2024. IEEE. ISBN 979-8-3503-5300-6. doi:10.1109/CVPR52733.2024.00461.
- Alec Radford, Jong Wook Kim, Chris Hallacy, Aditya Ramesh, Gabriel Goh, Sandhini Agarwal, Girish Sastry, Amanda Askell, Pamela Mishkin, Jack Clark, Gretchen Krueger, and Ilya Sutskever. Learning Transferable Visual Models From Natural Language Supervision, February 2021.
- Hemang Shah. 2007 BP Anisotropic Velocity Benchmark. BP Exploration Operation Company Limited ("BP"), 2007.
- Ross Wightman. PyTorch Image Models, 2019.
- Ruslan Kuprieiev, skshetry, Peter Rowlands, Dmitry Petrov, Paweł Redzyński, Casper da Costa-Luis, David de la Iglesia Castro, Alexander Schepanovski, Ivan Shcheklein, Gao, Batuhan Taskaya, Jorge Orpinel, Fábio Santos, Daniele, Ronan Lamy, Aman Sharma, Zhanibek Kaimuldenov, Dani Hodovic, Nikita Kodenko, Andrew Grigorev, Earl, Nabanita Dash, George Vyshnya, Dave Berenbaum, maykulkarni, Max Hora, Vera, and Sanidhya Mangal. DVC: Data Version Control - Git for Data & Models. Zenodo, January 2025.

A Appendix

A.1 Correlation between metrics and between tasks

	Correlation
Demultiple	
PSNR(Demultiple),SSIM(Demultiple)	0.9853
SSIM(Demultiple),MSE(Demultiple)	-0.9853
PSNR(Demultiple),MSE(Demultiple)	-1
Interpolation	
PSNR(Interpolation),SSIM(Interpolation)	1
SSIM(Interpolation),MSE(Interpolation)	-1
PSNR(Interpolation),MSE(Interpolation)	-1
Denoise	
PSNR(Denoise),SSIM(Denoise)	0.9853
SSIM(Denoise),MSE(Denoise)	-0.9853
PSNR(Denoise),MSE(Denoise)	-1
Between tasks	
PSNR(Demultiple),PSNR(Interpolation)	0.8922
PSNR(Demultiple),PSNR(Denoise)	0.9363
PSNR(Interpolation),PSNR(Denoise)	0.9583

Table 2: Correlation between metrics and between tasks.

All plots in this paper present a single metric, despite the fact that the PSNR, the SSIM and the MSE were measured for every experiment during the course of this investigation. This is due to the fact that these metrics are highly, and at times, even perfectly correlated, as demonstrated in Table 2. The table also provides the actual numbers for the correlation between downstream tasks, as depicted in Figure 5.

A.2 Decoder

The present investigation focused on the architecture of the FM employed as an image encoder, with the architecture and hyperparameters of the decoder fixed for all experiments presented. Prior to this, a preliminary investigation into the optimal architecture and hyperparameters was conducted for the demultiple task, as illustrated in Figure 14. This figure contains two plots contrasting the achieved PSNR against the number of parameters of the decoder. The left plot corresponds to the results, when employing a Swin model as the encoder and the right plot corresponds to the results obtained when using a ConvNeXt model as the encoder.

The decoder architecture is characterized by the existence of skip connections, the type of convolution block and the up-sampling method. If a decoder has skip connections than similar to the right side of a UNet all four features extracted from the FM are up-sampled and combined iteratively. Conversely, in the absence of skip connections, only the final feature is up-sampled and processed.

As observed in the figure, skip connections and the hierarchical features they enable are crucial for achieving optimal results. While the performance discrepancy is less pronounced when employing a ConvNeXt as the image encoder there is still a discrepancy of approximately 5 dB that remains. When utilizing a Swin model as the encoder, the discrepancy increases to around 15 dB. These results are analogous to the results demonstrated in Figure 5, underscoring the significance of multiscale features for seismic processing.

The choice of convolution block has a less significant impact on performance but models with more modern ConvNeXt blocks instead of traditional double convolution blocks, consistently outperform their counterparts with fewer parameters. This corroborates the performance discrepancy found in our investigations between EfficientNet and ConvNeXt models. The final architectural component we investigated was the up-sampling mechanism. With some exceptions, bilinear up-sampling seems to outperform transposed convolutions with fewer parameters.

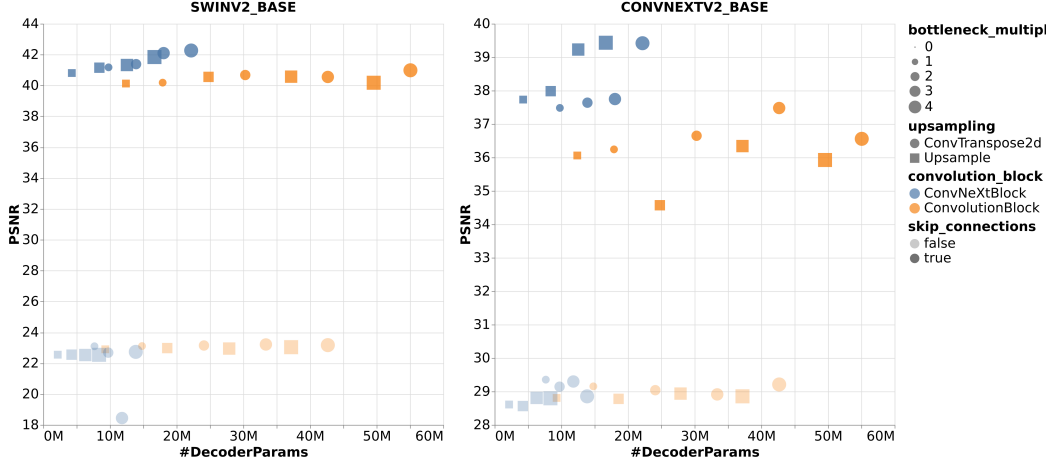


Figure 14: Hyperparameter analysis of the decoder.

After deciding on using skip connections, ConvNeXt blocks and bilinear up-sampling, the only hyperparameter left is the bottleneck multiplier in the convolution block. While increasing this led to consistent performance increases, a bottleneck multiplier of two was selected as a compromise between diminished performance and a more streamlined decoder. The advantage of a smaller decoder is that it shifts more responsibility to the encoder, the focal point of this investigation, and it reduces training time, thus enabling more experiments.

Also noteworthy is that the trends observed when employing a Swin model appear more linear, which could indicate more easily transferable features.

A.3 Variance

In the interest of conserving computational resources, all experiments, except for suspected outliers, were executed once. To verify the significance of the findings, the variance was measured using a Swin (V2) model for each training strategy. The average metrics and their standard deviations are presented in Table 3. As revealed in Figure 4, the best training strategy is *fine-tuned encoder*, followed by *non-pre-trained encoder* and lastly *frozen encoder*. Interestingly, the standard deviations of the metrics are significantly higher when strategy *fine-tuned encoder* was used.

	frozen encoder	non-pre-trained encoder	fine-tuned encoder
mean(PSNR)	41.10574405	44.48258406	44.65336791
std(PSNR)	0.05656527	0.04008933	0.14594771
mean(SSIM)	0.97927390	0.99004398	0.99054167
std(SSIM)	0.00027496	0.00007631	0.00035666
mean(MSE)	0.00035099	0.00016350	0.00015715
std(MSE)	0.00000470	0.00000156	0.00000505

Table 3: Variance of Swin (V2) trained five times with the different training strategies for the demultiple task.

A.4 Source Code

In addition to presenting our findings, we propose a framework for benchmarking FMs for seismic processing. All experiments described in this paper can be replicated without modifying the source code by adjusting parameters in the *params.yaml* file. Furthermore, DVC (developed by Kupriev et al. [2025]) was utilized to track the experiments, ensuring that the parameters and recorded metrics from all individual experiments are available via Git. This should further facilitate the ease of recreation and maybe the additional data can lead to further insights.

```
1 CONVNEXT_BASE: TimmBackboneConfig = TimmBackboneConfig(  
2     model_name="convnext_base.fb_in1k",  
3     features=(0, 1, 2, 3),  
4     n_channels=(128, 256, 512, 1024),  
5     down_sampling_rates=(4, 2, 2, 2),  
6     input_size_inference_behavior= InputSizeInferenceBehavior.VARIABLE,  
7     input_size=(256, 256),  
8     input_channels=3,  
9     channel_format=(ChannelFormat.NCHW, ChannelFormat.NCHW,  
10    ↪ ChannelFormat.NCHW, ChannelFormat.NCHW),  
11    metadata=Metadata(dataset="ImageNet-1k",  
    ↪ training_protocol=TrainingProtocol.SUPERVISED,  
    ↪ n_parameters=87564416),  
11 )
```

Listing 1: Example of the config for the ConvNeXt BASE model.

Aside from just recreating our experiments the library was designed for broad extensibility. Further datasets and tasks can easily be added. Furthermore, slotting in other models implemented in timm [Wightman, 2019] is as simple as adding an entry to the enum containing the configs. An example config for the ConvNeXt BASE model is shown in Listing 1. While models already implemented in timm are the most straightforward to incorporate, the addition of custom models is also feasible with minor alterations to the source code.

For more details and examples on how to utilize the library, please refer to the source code available at <https://codeberg.org/fuchsfa/foundation-models-seismic-processing>.